

Regulated Breathing Effect of Silicon Negative Electrode for Dramatically Enhanced Performance of Li-Ion Battery

Xingcheng Xiao,* Weidong Zhou, Youngnam Kim, Ill Ryu, Meng Gu, Chongmin Wang, Gao Liu, Zhongyi Liu, and Huajian Gao*

Si is an attractive negative electrode material for lithium ion batteries due to its high specific capacity ($\approx 3600 \text{ mAh g}^{-1}$). However, the huge volume swelling and shrinking during cycling, which mimics a breathing effect at the material/electrode/cell level, leads to several coupled issues including fracture of Si particles, unstable solid electrolyte interphase, and low Coulombic efficiency. In this work, the regulation of the breathing effect is reported by using Si-C yolk-shell nanocomposite which has been well-developed by other researchers. The focus is on understanding how the nanoscaled materials design impacts the mechanical and electrochemical response at electrode level. For the first time, it is possible to observe one order of magnitude of reduction on breathing effect at the electrode level during cycling: the electrode thickness variation reduced down to 10%, comparing with 100% in the electrode with Si nanoparticles as active materials. The Si-C yolk-shell nanocomposite electrode exhibits excellent capacity retention and high cycle efficiency. In situ transmission electron microscopy and finite element simulations consistently reveals that the dramatically enhanced performance is associated with the regulated breathing of the Si in the new composite, therefore the suppression of the overall electrode expansion.

1. Introduction

Li-ion batteries have attracted much interest from both academia and industry for applications in vehicular propulsion, portable electronic devices, and stationary energy storages due to their high energy density. Among the various anode materials for Li-ion batteries, Si is a promising candidate to replace

graphite because of its high theoretical capacity (10 times higher than graphite at $\approx 3600 \text{ mAh g}^{-1}$), low working potential, abundance, and environmentally benign manufacturing process.^[1,2] A major hurdle to the practical application of Si electrode is the large volume expansion and contraction (up to 300%) during charging and discharging processes, which causes a variety of issues such as pulverization of Si particles, fracture of electrode, unstable solid-electrolyte interphase (SEI), and poor electrode integrity. Here we report that the cell breathing effect associated with large volume change is a major contributing factor to the performance degradation of Si-containing Li-ion batteries. The term “breathing” is used to indicate the cyclic volume change, particularly the thickness of the cell during battery operation.

The structural degradation of the Si electrode, including cracking and pulverization, caused by large volume changes provokes catastrophic fast capacity fading.^[3] In addition, continuous formation of new SEI layers on fractured surfaces leads to low Coulombic efficiency.^[4] Various nanostructured electrodes have been proposed to address these problems, including Si nanocrystals, nanofibers, nanotubes, nanospheres, and nanoporous materials,^[5–16] with improved performances compared to bulk or micrometer-sized electrodes. Novel binders, electrolyte additives, and conductive additives including graphite, amorphous carbon, carbon nanotubes, carbon nanofibers, graphene, and metals have also been proposed to overcome the intrinsic limits of bulk Si.^[17–25]

A major limitation of the above approaches is the difficulty to generate stable SEI and to achieve stable electrochemical cycling performance for realistic applications.^[26] The SEI layer formed on nanostructured Si is not stable because it has to go through substantial expansion and contraction along with Si during cycling, which likely results in buckling, fracture, and delamination of SEI from the Si surface. As a result, new SEI will continuously form, leading to irreversible capacity loss and low current efficiency. To stabilize the SEI layer, different surface coatings, including metal oxide coatings prepared by atomic layer deposition^[27,28] as well as C-coating by chemical vapor deposition,^[29] have been deposited on Si surface. However, despite enhanced electrochemical performances such as cycle stability and efficiency, those coatings coating cannot withstand the large volume changes of Si during discharge/charge cycles.

Dr. X. Xiao, Dr. W. Zhou, Y. Kim, Z. Liu
General Motors Global Research & Development Center
Warren, MI 48090, USA
E-mail: xingcheng.xiao@gm.com

Dr. I. Ryu, Prof. H. Gao
School of Engineering
Brown University
Providence, RI 02912, USA
E-mail: Huajian_Gao@brown.edu

Dr. M. Gu, Dr. C. Wang
Environmental Molecular Sciences Laboratory
Pacific Northwest National Laboratory
Richland, WA 99352, USA

Dr. G. Liu
Lawrence Berkeley National Laboratory
1 Cyclotron Rd, Berkeley, CA 94720, USA



DOI: 10.1002/adfm.201403629

We demonstrate in this paper that the breathing effect associated with the Si electrode volume change is a major factor negatively impacting electrode integrity and the reliability of a battery pack. As electrode materials are normally tested in a coin cell format with a stainless steel case, their volume expansion is of little concern. The coin cell format, however, is not a real representation of the actual cell configuration in a battery pack. In practice, the large volume expansion of Si electrodes causes noticeable pouch cell “breathing.” It not only leads to the poor electrode integrity, but also generates large stress and strain to the cell tabs.

To address the breathing effect, we adopted Si–C yolk–shell nanoparticles with free space between Si and C to mitigate the detrimental impacts of Si volume expansion on both the electrode and the battery pack. Similar yolk–shell structures have been recently reported by several groups with significantly improved electrochemical performance,^[16,29,33] and their pioneer work have demonstrated the cycle stability and current efficiency can be significantly improved by designing such nanostructure. Inspired by the promising performance from the yolk–shell structure, we further investigate how the materials design at nanoscale impacts the mechanical and electrochemical behaviors at electrode level. With the aid of in situ TEM and electrochemical dilatometer measurement, we clearly demonstrated how free space in Si–C yolk–shell can effectively minimize the volume expansion of Si based electrode and suppress the pouch cell breathing effect. This finding was further elucidated by finite element modeling.

2. Results

Figure 1 depicts a representative TEM image of a single Si–C yolk–shell particle, which clearly shows the free space between Si core and C shell, and that of the associated nanocomposite made of Si–C yolk–shell particles. This unique structure provides excellent capacity retention and cycling efficiency, as shown in **Figure 2**. The specific capacity for each electrode is calculated based on the total mass, including that from carbon shell in case of Si–C shell and yolk–shell Si. We made sure that the average pure Si mass loading for each electrode is around 1 mg cm^{-2} , so we could have the fair comparison. The Si–C nanocomposite exhibited a high capacity of $\approx 1430 \text{ mAh g}^{-1}$ after formation cycles (based on the weight of Si–C nanocomposite), higher Coulombic efficiency, and stable cycling ($\approx 85\%$ capacity retention over 100 cycles). It should be noted that in the electrochemical tests, the first three cycles were tested under a slow C rate of C/50 as activation/formation cycles. The remaining cycles were charged/discharged at C/10. For comparison, an electrode made of bare Si nanoparticles showed much faster capacity fading and lower Coulombic efficiency. These results are similar to previous studies,^[13,14,25] where improved cycling stability was obtained by creating yolk–shell.

It is important to note that, from a fracture point of view, the nanosized Si particle should have much better cycle performance than that shown in **Figure 2**, because the particle size is under its critical value for fracture. Apparently, unstable SEI has led to low cycle efficiency and quick mechanical degradation in spite of the small particle size. Although the Si–C core

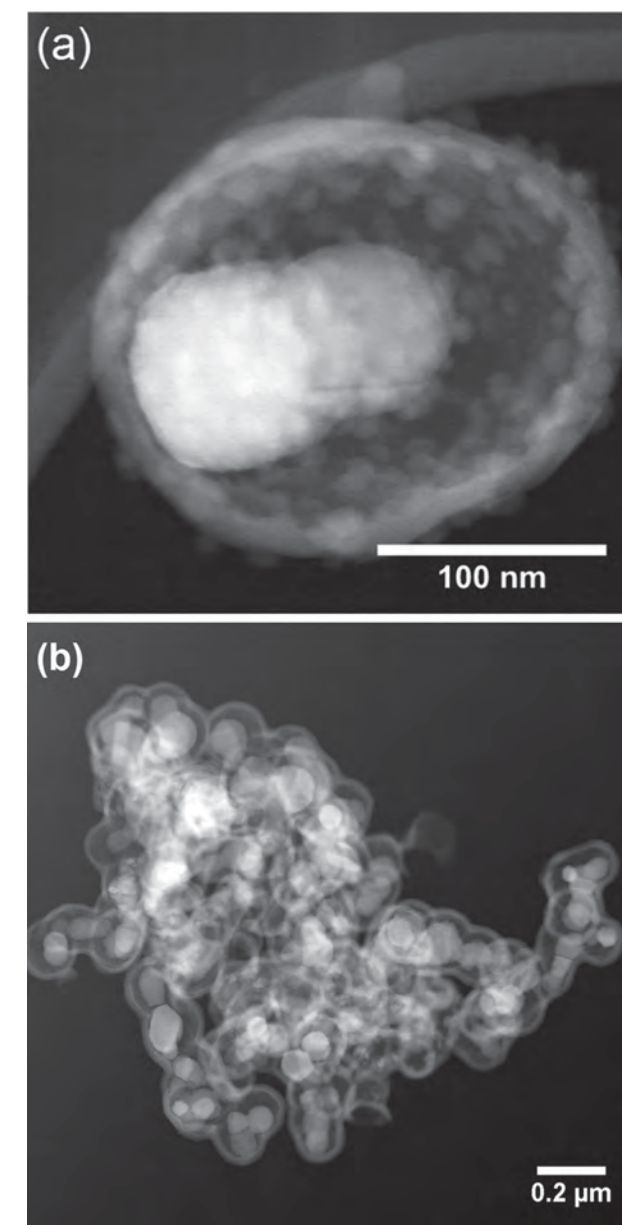


Figure 1. Morphologies of a Si–C yolk–shell structure and the associated nanocomposite. a) A single Si–C hollow yolk–shell nanoparticle, and b) associated Si–C nanocomposite.

shell electrode can improve the cycle performance, it cannot accommodate the huge volume expansion and contraction, nor can it address the issue of electrode integrity for long term cycle performance. In comparison, the good cycling stability of the Si–C yolk–shell nanocomposite electrode can be attributed to the unique structure containing void space which mitigates both chemical and mechanical degradation during charge/discharge process. In the yolk–shell structure, Si is isolated by the carbon shell, and SEI on the carbon shell has much less volume expansion. As a result, the SEI layer on the C shell can be stabilized without going through huge volume expansion and contraction. The stabilized SEI in turn prevents electrolyte decomposition reactions that typically occur on newly fractured

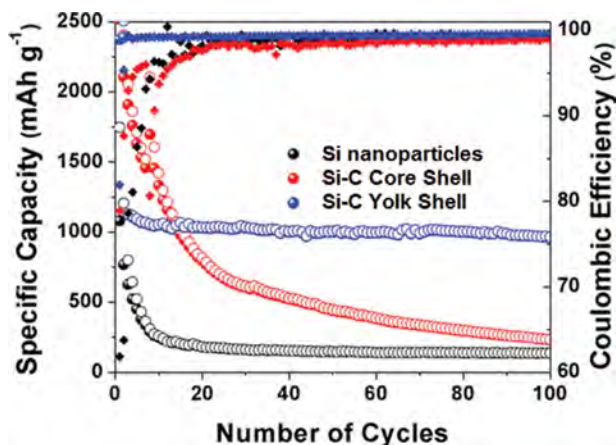


Figure 2. Electrochemical behaviors of Si nanoparticles and Si-C yolk-shell nanocomposite.

surfaces exposed to the electrolyte. Simultaneously, the electrical conductivity of the C shell reduces the internal resistance of the whole electrode. These factors contribute to the measured low electrochemical impedance shown in Figure 3. The diameter (representing inter-particle contact resistance) of the Si-C nanocomposite semicircle is clearly smaller than that of the bare Si nanoparticles and it maintains the same value after the 10th cycle, suggesting that the C coating suppressed inter-particle contact resistance and result in better cycling performance. Also, the substantial impedance increase of Si nanoparticle after 10 cycles is another indication of continuous SEI formation due to large volume expansion and contraction.

The most critical contribution from the yolk-shell architecture is the free space accommodating the volume expansion, which not only stabilizes the SEI layer but also suppresses the breathing effect and minimizes its negative impact on electrode integrity. We used the in situ electrochemical dilatometer to capture the thickness change of the electrode under different states of lithiation/delithiation.^[30,31] The results are shown in Figure 4. The electrodes swell in discharging and contract in

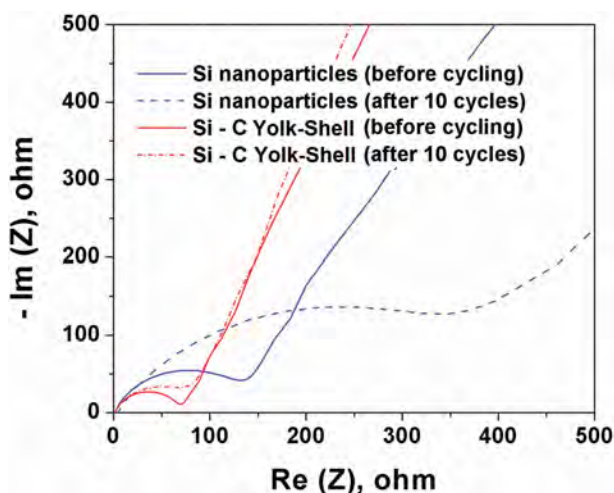


Figure 3. Electrochemical Impedance Spectroscopy (EIS) of Si nanoparticles and Si-C yolk-shell nanoparticles.

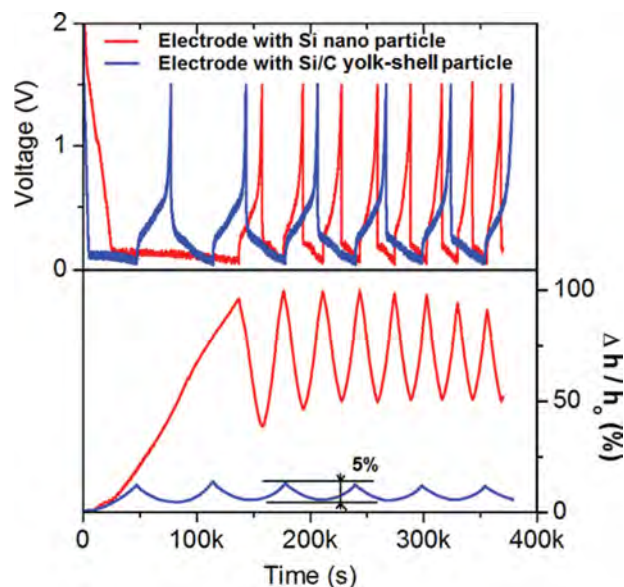


Figure 4. Electrode thickness variation of the electrode with Si nanoparticles (red curves) and Si-C yolk-shell nanoparticles (blue curves), by in situ electrochemical dilatometer measurement.

charging. The Si nanoparticle electrodes exhibit 40% to 50% thickness changes in normal cycling, even though the electrode itself contains 50% porosity and soft polymer binder. This huge breathing effect on Si nanoparticle electrodes would be a serious problem in real applications, particularly when tens of electrode films are assembled into a pouch cell and hundreds of pouch cells are assembled into a battery pack. In contrast, the yolk-shell structure reduces the breathing effect down to 5%. Apparently, most of the volume expansion from Si has been confined in the C shell. We believe this architecture would significantly simplify both the electrode and battery pack design. Another interesting phenomenon we observed is that the irreversible electrode expansion at the first cycle is quite different in both cases. For the electrode made of Si nanoparticles, the irreversible change of electrode thickness is not only from the Si particle itself, but also from the large amount of SEI formed on the relatively large surface area based on the low first cycle efficiency. In contrast, there is much less irreversible change from the yolk-shell structure with free space mainly due to the stabilized SEI layer as well as the reduced surface area.

In the processing of the yolk-shell structure, it is easy to control the free space by controlling the thickness of the sacrificial layer. However, due to the size distribution of Si nanoparticles, it is difficult to make sure that the free space is always just enough to accommodate the volume expansion from each Si nanoparticle, without the compromise of volumetric capacity otherwise. To address this issue, we considered two representative scenarios: in one case the volume of Si core is 3 or 4 times smaller than that of inner space of the carbon shell. In situ TEM results demonstrate that Si expands inside the shell without causing any expansion of the C shell, as shown in Figure 5.^[32–35] The other case is that the space is not enough to accommodate the volume expansion from Si particle. Figure 6 displays images captured from the video in the Supporting Information, which clearly show the C shell

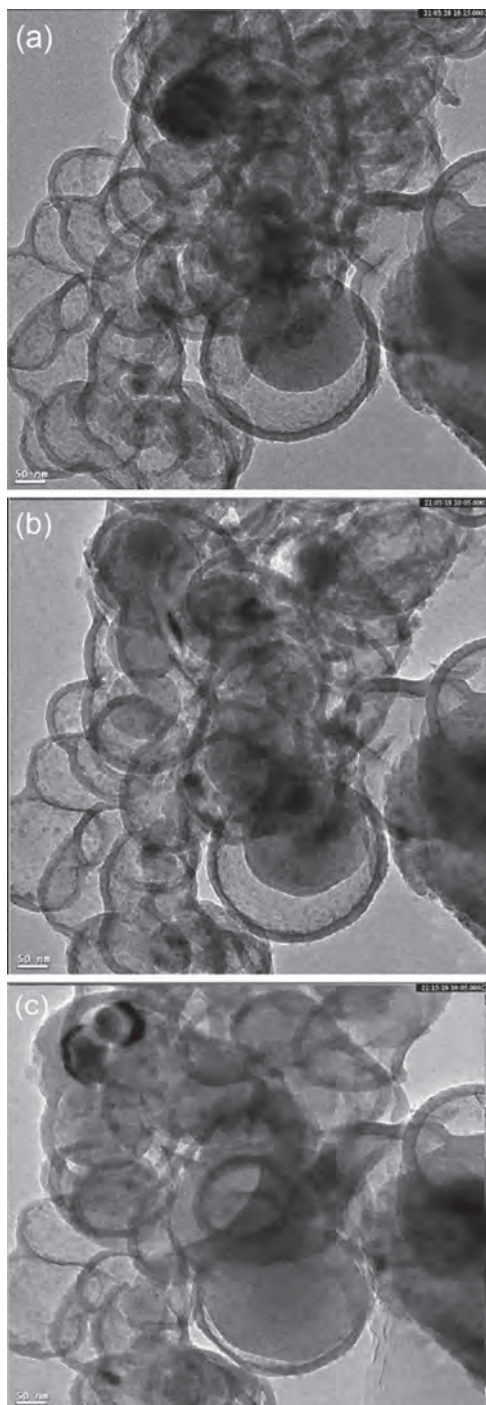


Figure 5. In situ TEM images showing the volume expansion of a Si nanoparticle inside a carbon shell: The free space is large enough to accommodate Si volume expansion. The whole volume expansion process is shown in the Supporting Information, Movie 1.

still has negligible volume expansion even though the lithiated Si has fully filled all the inner space of the shell. These results indicate that most of the volume expansion has been confined in the carbon shell, which explains why the yolk-shell nanostructure can suppress the breathing effect at the electrode level.

3. Simulations

Our experimental observation raised an important question. How does the C shell suppress the volume expansion and breathing effect when the free space is not large enough to accommodate the volume expansion of Si particle? To address this question, we have conducted finite element simulation of the lithiation of an amorphous Si particle inside a C shell. Recent experiments have shown that lithiation in amorphous Si proceeds in a two phase reaction during the initial cycle, and after the first cycle it is expected to be driven by diffusion.^[36,37] Based on these findings, we adopted slightly different models for the initial and subsequent cycles. In our simulation, an analogy between heat transport and mass diffusion is used, with temperature corresponding to a normalized concentration and thermal expansion to concentration-induced volume expansion. During lithiation/delithiation, the Si core undergoes large volume changes, accompanied by elastic and plastic deformation in the confined environment. For the plastic deformation, the von Mises criterion is used to determine yielding, and plastic strain is governed by the J_2 -flow rule. Material properties and parameters used in the model are listed in Table 1 of the Supporting Information. The following galvanostatic boundary condition is imposed on the surface of the Si particle,

$$J = J_0(1 - c) \quad (1)$$

where J_0 is the initial flux and c the normalized concentration.

In the model for the first cycle, we used the large deformation J_2 -flow theory to model plastic deformation and solved the expansion/elastic/plastic deformation separately from diffusion equation. For the diffusion part, we follow Liu et al.^[32] to model the propagation of discrete phase boundary between pure amorphous Si and lithiated Li_xSi compound by treating the diffusivity as a nonlinear function of local Li concentration, while taking into account the effect of internal stress on the diffusional energy barrier.^[38] In doing so, the diffusivity was written as

$$D = D_0 \left[\frac{1}{1 - c} - 2\Omega c \right] e^{\alpha V_p \sigma_b / RT} \quad (2)$$

where D_0 is a reference diffusivity and Ω is the enthalpic component of the free energy of formation for the Li_xSi compound; V_p is the partial molar volume of Li in Li_xSi , α is a constant taking to be around 0.5 (see Table 1) and σ_b is the biaxial stress in the direction normal to the direction of diffusion flux.

For the subsequent cycles, we modeled lithiation in the yolk-shell using a fully coupled, large deformation framework by An and Jiang,^[39] which includes the effect of pressure gradient on diffusion and its corresponding large volume expansion. The resultant flux in the reference configuration is expressed as

$$\tilde{J} = - \left\{ \left[\frac{1}{1 - c} + \frac{3\beta^2 c \det F \sigma_h}{(1 + \beta c)^2} \right] \frac{\partial c}{\partial \tilde{x}} - \frac{3\beta c}{1 + \beta c} \frac{\partial}{\partial \tilde{x}} (\det F \sigma_h) \right\} e^{\alpha V_p \sigma_b / RT} \quad (3)$$

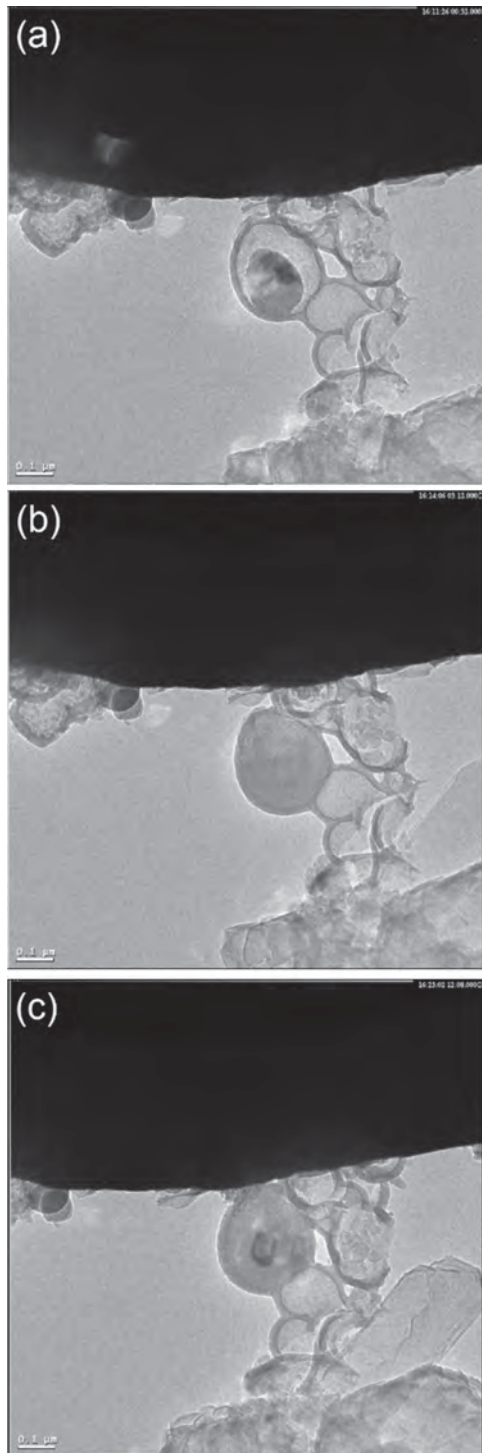


Figure 6. In situ TEM images showing the volume expansion of a Si nanoparticle inside a carbon shell when the free space is not large enough to accommodate Si volume expansion. In this case, the C shell is still capable of constraining the volume expansion of Si particle inside. The whole volume expansion process is shown in the Supporting Information, Movie 2.

where β is the compositional linear expansion coefficient; σ_h , $\det F$ are the hydrostatic stress and deformation gradient, respectively; the exponential term is introduced here to capture

Table 1. Material properties and operating parameters.

Material	Description	Symbol [dimension]	Value
Si core (amorphous)	Young's modulus	E^{Si} [GPa]	185
	Poisson's ratio	ν^{Si} [-]	0.28
	Yield stress	s_y^{Si} [GPa]	7
	Constant	α [-]	0.5 ^{a)}
	Expansion coefficient	β [-]	0.442
	Max. Li concentration	C_{max} [mole m^{-3}]	0.3667×10^6
C shell	Constant	Ω [-]	2
	Young's modulus	E^{C} [GPa]	1000
Parameters	Poisson's ratio	ν^{C} [-]	0.22
	Gas constant	R [J $\text{K}^{-1} \text{mole}^{-1}$]	8.314
	Temperature	T [K]	300
	Diffusivity	D_0 [$\text{cm}^2 \text{s}^{-1}$]	10^{-12}
	Characteristic length	L [nm]	1

^{a)}This value is assumed from the diffusion of H in Ni, where α ranges from 0.180 under compression to 0.404 under tension.^[36]

the effect of internal stress on the diffusional energy barrier.^[38] In this expression, a dimensionless formulation is used: stress is normalized by $C_{\text{max}}RT$ and flux is normalized $C_{\text{max}}D_0/L$ (See Table 1 for the meanings of these symbols). In our simulation, the Si core has a radius of 75 nm and the C shell has an inner radius of 85 nm and outer radius of 105 nm, following the TEM image in Figure 6.

In both models, it was found that there is no significant change in total volume of the hollow core-shell structure even after the Si core expands to fill the empty space between the core and shell, in agreement with the experimental observation shown in Figure 4. Our simulations indicate that the primary reason for volume preservation is because the confining stress due to the C shell has stopped the Si core from achieving full lithiation through the exponential term in Equations (2),(3). To illustrate this more clearly, we considered the same model for lithiation during the initial cycle but without the exponential term for the effect of internal stress on diffusion. In this case, our simulations showed substantial volume expansion ($\approx 20\%$) of the yolk-shell structure in spite of the mechanical constraint from the C shell (Supporting Information, Movie 3).

Due to the coupling between internal stress and diffusivity in both models, lithiation essentially stopped after the Si core expands to fill all the free space between the Si core and C shell. This can be clearly seen in Figures 7B,D, where the lithium concentration profiles cease to change significantly shortly after the free space is filled by the expanding core at ≈ 200 s for the initial cycle and ≈ 100 s into the subsequent cycles. The large compressive stress induced by the C shell raises the activation energy for diffusion in Si, which hinders further lithiation of the core and stops the associated volume expansion. **Figure 7** plots the evolution of the normalized concentration profile during lithiation for the initial (a,b) and subsequent cycles (c,d). These modeling results thus laid a theoretical support for our experimental observation (Figure 6c)

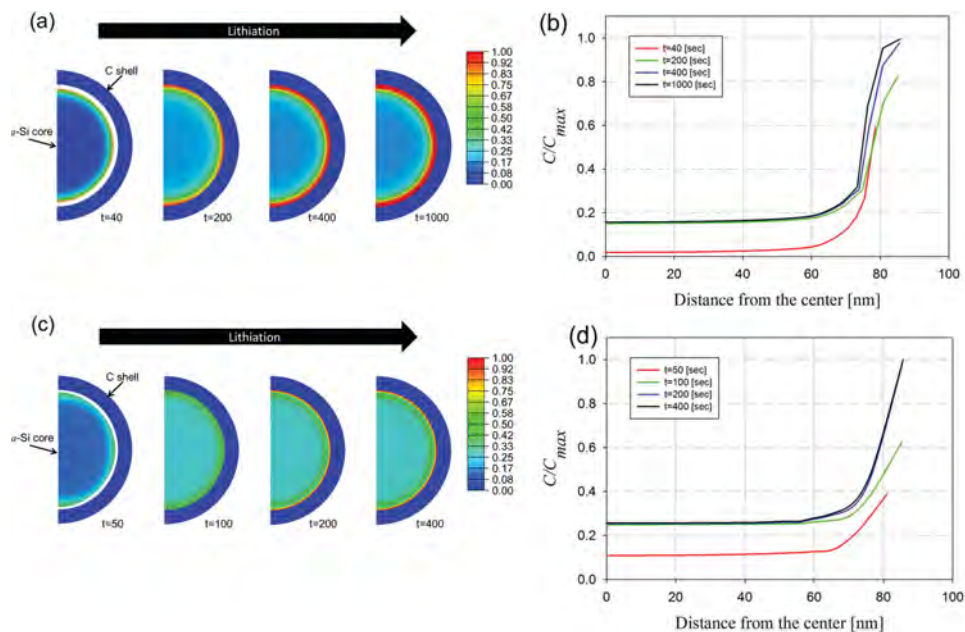


Figure 7. Finite element simulations of lithiation in a Si–C yolk–shell structure. Evolution of the morphology and normalized Li concentration in the yolk–shell structure during lithiation in the initial (a,b) and subsequent cycles (c,d). Detailed concentration evolutions can also be seen in the Supporting Information, Movies 4, 5.

that the free space in Si–C yolk–shell structure suppresses the volume expansion of the Si core and minimizes the associated breathing effect.

4. Conclusions

By adopting a free space in the Si–C yolk–shell structure in which a Si nanoparticle is encapsulated in a carbon shell, some critical issues with using Si as anode material in Li-ion batteries, such as the loss of electrical contact and unstable SEI caused by huge volume changes, are substantially alleviated so that high cycle stability and efficiency can be achieved. Most importantly, the breathing effect in Si based electrode has been significantly suppressed. The in situ electrochemical dilatometer measurement, combined with in situ TEM, clearly shows that the Si volume expansion has been confined inside of the shell, which is further clarified by the coupling effect of confining stress of the C shell and lithium diffusivity in silicon. It has been demonstrated the yolk–shell structure presents a promising approach to designing Si based negative electrode. Although the introduced free space might compromise the volumetric energy density, it might be possible to reduce the overall porosity of the whole electrode to compensate that loss, which will be further investigated in the future.

5. Experimental Section

Fabrication of Yolk–Shell Particles: Concentrated ammonium hydroxide 3.0 mL were added into a dispersion of 300 mg Si nanoparticles (with average particle size around 100 nm in diameter) in 400 mL mixture

of Ethanol/Water (3:1) under vigorous stirring. 4 g of tetraethoxysilane (TEOS) was introduced dropwise and the mixture was stirred at room temperature for 12 h. The suspension was then centrifuged, rinsed and dried to yield slightly brown particles of Si@SiO₂. The obtained Si@SiO₂ was dispersed into the DMF solution of polyacrylonitrile under sonication for 3 h to yield a brown suspension, which was then slowly added into excess pure water containing 2% Polyvinylpyrrolidone (PVP, 40000) under strong stirring to form polyacrylonitrile coated Si@SiO₂ after centrifugation. After that, the obtained polyacrylonitrile coated Si@SiO₂ was heated at 700 °C for 2 h in the presence of argon flow to carbonize the polymer and give the carbon coated Si@SiO₂. Another approach to coat carbon is using thermal carbonization of polystyrene. Polystyrene suspended in dimethylformamide (DMF) was adsorbed onto the SiO₂–Si particles as carbon precursor and carbonized by heating the mixture to 700 °C for 30 min under H₂ formation gas. Finally, the carbon coated Si@SiO₂ particles were dispersed in 3% HF solution and stirred for 1 h, followed by centrifugation and rinsing with water, to obtain the yolk–shell structure.

TEM Characterization: The morphology and nanostructure of the Si–C nanocomposite at each step of the synthesis were examined with transmission electron microscopy (TEM). The TEM used in this work was an aberration-corrected JEOL 2100F microscope operated at 200 kV. The C surface coating was analyzed by Raman spectroscopy (ThermoScientific, Thermo Nicolet Almega System). The amount of Si in the Si–C nanocomposite was determined by thermo gravimetric analysis (TGA) (Netzsch, QMS 403/5 SKIMMER).

Electrode Preparation and Measurement: To prepare the electrodes, the Si-based materials were mixed with carbon black and sodium alginate binder (80:10:10 wt%) in deionized water to form slurry. The slurry was coated on copper foil, dried in a vacuum oven at 120 °C for overnight and pressed to enhance contact between the active materials and conductive carbon. The mass loading of Si nanoparticles is around 1 mg cm⁻². The electrode thicknesses for different electrodes range from 20 to 50 μm. All electrochemical tests were performed via coin cell testing platform. Microporous membrane (Celgard, USA) was used as the separator; 1 M LiPF₆ in a mixed solution of ethylene carbonate and diethyl carbonate (1:1 volume ratio, Novolyte, USA) with 10 wt% fluoroethylene carbonate (FEC) as the additive was selected as the electrolyte. The

thickness change of electrodes during cycling was measured using an electrochemical dilatometer (EL-Cell, Germany). The electrolyte was the same used in the coin cell. The biologic VMP3 potentiostat was used to cycle the electrode.

In Situ TEM: For the in situ TEM experiment, the procedure used in this work is similar to that as previously reported.^[40] A piece of the electrode material was attached to a phosphorus-doped silicon nanowire, which was bonded to a gold rod using conductive epoxy. A piece of lithium metal was attached to a tungsten rod served as the counter electrode. A thin layer of Li₂O formed on the lithium metal surface acts as the solid electrolyte in the nanobattery. The nanobattery is placed into the TEM column for in situ dynamical observation. Application of proper potential (≈ 2 V) was used to drive the lithiation and delithiation processes. The loading of the sample in the microscope was performed using an Ar-filled glove bag. The total air exposure during the loading of the sample into the microscope was less than 2 s. All the in situ electrochemical tests were conducted on a Titan 80–300 kV scanning/transmission electron microscope (S/TEM) operated at 300 kV with a Nanofactory TEM scanning tunneling microscopy (STM) holder. The EELS spectra are taken with a Quantum model Gatan Image Filter with a 2 k*2 k pixel CCD.

Simulation: Commercial finite element package ABAQUS was used in our simulations of the lithiation of a Si particle inside a C shell. In solving the diffusion problem, we made use of the coupled analysis module in ABAQUS for heat transfer problems together with user-defined subroutines UMATHT, UMAT, DFLUX, USDFLD, and UEXPAN. For the initial charging, the concentration and stress dependent diffusivity (Equation (2)) was implemented using the user-subroutines. For simplicity, the stress values were saved in the USDFLD subroutine at the previous time step and passed to the UMATHT subroutine to compute the diffusion flux at current time step. The maximum time step was kept to less than 10^{-6} of the total simulation time, without causing significant loss in accuracy. In addition, due to the large volume expansion during lithiation (used in the UEXPAN subroutine), the relation between the partial molar volume and fictitious thermal expansion coefficient was modified as:^[41]

$$\beta = \frac{1}{3} \frac{V_p}{1 - cV_p} \quad (4)$$

The galvanostatic boundary condition was implemented in the DFLUX subroutine in all simulations. For the subsequent charging cycles, the diffusional flux expression in Equation (3) was implemented in the UMATHT subroutine, in which the following terms need to be defined: heat capacity per volume, and heat flux and its derivatives with respect to temperature and temperature gradient. Calculation of other terms were relatively straightforward, but the gradients of stress and deformation (i.e., $\partial(\sigma_h, \sigma_h \det F)/\partial x$ in Equation (3) were quite challenging. To compute the spatial gradient of $\sigma_h \det F$, its values at neighboring elements need to be accessible, but the data passed to UMATHT subroutine is only at its own integration points. We computed this gradient term via the pointwise least square method. Specifically, the data for second nearest neighboring elements were stores in the common block to be accessible when the subroutine was called. Assuming linear distribution of $\sigma_h \det F$ in an element, its gradient is computed using the least square method. In principle, this gradient term can also be computed via interpolation using shape functions, but the fluctuation of stress from numerical errors can cause convergence problem, especially at high lithium concentrations. In addition, we used the UEXPAN and DFLUX subroutines similar to the initial cycle.

Acknowledgements

All authors contributed equally to this work. The authors would like to thank Dr. Yue Qi, Dr. Qiangfeng Xiao, Dr. Mei Cai, Dr. Mark Verbrugge at

GM R&D for valuable discussions. The authors also acknowledges the support by the Assistant Secretary for Energy Efficiency and Renewable Energy, Vehicle Technologies Office of the U.S. Department of Energy under Contract No. DE-AC02-05CH11231, Subcontract No 7056410 under the Batteries for Advanced Transportation Technologies (BATT) Program. I.R. and H.G. also acknowledge support by U.S. Department of Energy through DOE EPSCoR Implementation Grant No. DE-SC0007074 and the GM/Brown CRL on Computational Materials Science. M.G. and C.M.W. acknowledge the support of Chemical Imaging Initiative at Pacific Northwest National Laboratory (PNNL), which was conducted in the William R. Wiley Environmental Molecular Sciences Laboratory (EMSL), a national scientific user facility sponsored by DOE's Office of Biological and Environmental Research and located at PNNL.

Received: October 16, 2014

Revised: November 26, 2014

Published online:

- [1] B. A. Boukamp, G. C. Lesh, R. A. Huggins, *J. Electrochem. Soc.* **1981**, 128, 725.
- [2] M. T. McDowell, S. W. Lee, W. D. Nix, Y. Cui, Understanding the Lithiation of Silicon and Other Alloying Anodes for Lithium-Ion Batteries (25th Anniversary Article). **2013**, 25, 4966.
- [3] S. J. Lee, J.-K. Lee, S.-H. Chung, H.-Y. Leeb, S.-M. Leeb, H.-K. Baik, *J. Power Sources* **2001**, 97, 191.
- [4] H. Wu, G. Zheng, N. Liu, T. J. Carney, Y. Yang, Y. Cui, *Nano Lett.* **2012**, 12, 904.
- [5] H. Kim, M. Seo, M. H. Park, J. Cho, *Angew. Chem. Int. Ed.* **2010**, 49, 2146.
- [6] L. F. Cui, Y. Yang, C. M. Hsu, Y. Cui, *Nano Lett.* **2009**, 9, 3370.
- [7] R. Teki, M. K. Datta, R. Krishnan, T. C. Parker, T.-M. Lu, P. N. Kumta, N. Koratkar, *Small* **2009**, 5, 2236.
- [8] H. Ma, F. Cheng, J.-Y. Chen, J.-Z. Zhao, C.-S. Li, Z.-L. Tao, J. Liang, *Adv. Mater.* **2007**, 19, 4067.
- [9] M. H. Park, M. G. Kim, J. Joo, K. Kim, J. Kim, S. Ahn, Y. Cui, J. Cho, *Nano Lett.* **2009**, 9, 3844.
- [10] N. Liu, Z. Lu, J. Zhao, M. T. McDowell, H.-W. Lee, W. Zhao, Y. Cui, *Nat. Nanotechnol.* **2014**, 9, 187.
- [11] C. K. Chan, R. N. Patel, M. J. O'Connell, B. A. Korgel, Y. Cui, *ACS Nano* **2010**, 4, 1443.
- [12] M. H. Park, M. G. Kim, J. Joo, K. Kim, J. Kim, S. Ahn, Y. Cui, J. Cho, *Nano Lett.* **2009**, 9, 3844.
- [13] L.-F. Cui, R. Ruffo, C. K. Chan, H. Peng, Y. Cui, *Nano Lett.* **2009**, 9, 491.
- [14] C. K. Chan, H. Peng, G. Liu, K. McIlwrath, X. F. Zhang, R. A. Huggins, Y. Cui, *Nat. Nanotechnol.* **2008**, 3, 31.
- [15] S. Chen, M. L. Gordin, R. Yi, G. Howlett, H. Sohn, D. Wang, *Phys. Chem. Chem. Phys.* **2012**, 14, 12741.
- [16] R. Yi, F. Dai, M. L. Gordin, S. Chen, D. H. Wang, *Adv. Energy Mater.* **2013**, 3, 295.
- [17] R. Yi, F. Dai, M. L. Gordin, H. S. Sohn, D. H. Wang, *Adv. Energy Mater.* **2013**, 3, 1507.
- [18] C. Wang, H. Wu, Z. Chen, M. T. McDowell, Y. Cui, *Nat. Chem.* **2013**, 5, 1042.
- [19] H. Wu, G. Yu, L. Pan, N. Liu, M. T. McDowell, Z. Bao, Y. Cui, *Nat. Commun.* **2013**, 4, 1943.
- [20] Y. Yu, L. Gu, C. Zhu, S. Tsukimoto, P. A. v. Aken, J. Maier, *Adv. Mater.* **2010**, 22, 2247.
- [21] N.-S. Choi, K. H. Yew, K. Y. Lee, M. Sung, H. Kim, S.-S. Kim, *J. Power Sources* **2006**, 161, 1254.
- [22] J. Xiao, W. Xu, D. Wang, D. Choi, W. Wang, X. Li, G. L. Graff, J. Liu, J.-G. Zhang, *J. Electrochem. Soc.* **2010**, 157, A1047.
- [23] J. K. Lee, K. B. Smith, C. M. Hayner, H. H. Kung, *Chem. Comm.* **2010**, 46, 2025.

- [24] W. Wang, M. K. Datta, P. N. Kumta, *J. Mater. Chem.* **2007**, *17*, 3229.
- [25] M. Wu, X. Xiao, N. Vukmirovic, S. Xun, P. K. Das, X. Song, P. Olalde-Velasco, D. Wang, A. Z. Weber, L.-W. Wang, V. S. Battaglia, W. Yang, G. Liu, *J. Am. Chem. Soc.* **2013**, *135*, 12048.
- [26] G. Liu, S. Xun, N. Vukmirovic, X. Song, P. Olalde-Velasco, H. Zheng, V. S. Battaglia, L. Wang, W. Yang, *Adv. Mater.* **2011**, *23*, 4679.
- [27] X. Xiao, P. Lu, D. Ahn, *Adv. Mater.* **2011**, *23*, 3911.
- [28] X. Meng, X. Yang, X. Sun, *Adv. Mater.* **2012**, *23*, 3589.
- [29] X. Li, P. Meduri, X. Chen, W. Qi, M. H. Engelhard, W. Xu, F. Ding, J. Xiao, W. Wang, C. Wang, J.-G. Zhang, J. Liu, *J. Mater. Chem.* **2012**, *22*, 11014.
- [30] N. Dimov, S. Kugino, M. Yoshio, *Electrochim. Acta* **2003**, *48*, 1579.
- [31] S. Park, T. Kim, S. M. Oh, *Electrochem. Solid-State Lett.* **2007**, *10*, A142.
- [32] X. H. Liu, H. Zheng, L. Zhong, S. Huang, K. Karki, L. Q. Zhang, Y. Liu, A. Kushima, W. T. Liang, J. W. Wang, J.-H. Cho, E. Epstein, S. A. Dayeh, S. T. Picraux, T. Zhu, J. Li, J. P. Sullivan, J. Cumings, C. Wang, S. X. Mao, Z. Z. Ye, S. Zhang, J. Yu, *Nano Lett.* **2011**, *11*, 3312.
- [33] N. Liu, H. Wu, M. T. McDowell, Y. Yao, C. Wang, Y. Cui, *Nano Lett.* **2012**, *12*, 3315.
- [34] M. Gu, Y. Li, X. Li, S. Hu, X. Zhang, W. Xu, S. Thevuthasan, D. R. Baer, J.-G. Zhang, J. Liu, C. Wang, *ACS Nano* **2012**, *6*, 8439.
- [35] M. Gu, Z. Wang, J. G. Connell, D. E. Perea, L. J. Lauhon, F. Gao, C. Wang, *ACS Nano* **2013**, *7*, 6303.
- [36] J. W. Wang, Y. He, F. Fan, X. H. Liu, S. Xia, Y. Liu, C. T. Harris, H. Li, J. Yu Huang, S. X. Mao, T. Zhu, *Nano Lett.* **2013**, *13*, 709.
- [37] M. T. McDowell, S. W. Lee, J. T. Harris, B. A. Korge, C. Wang, W. D. Nix, Y. Cui, *Nano Lett.* **2013**, *13*, 758.
- [38] H. Haftbaradaran, J. Song, W. A. Curtin, H. Gao, *J. Power Sources* **2011**, *196*, 361.
- [39] Y. An, H. Jiang, A finite element simulation on transient large deformation and mass diffusion in electrodes for lithium ion batteries, *Modelling Simul. Mater. Sci. Eng.* **2013**, *21*, 074007.
- [40] M. Gu, X. Xiao, G. Liu, S. Thevuthasan, D. R. Baer, J. Zhang, J. Liu, N. D. Browning, C. Wang, *Sci. Rep.* **4**, 3684.
- [41] I. Ryu, et al. Size-dependent fracture of Si nanowire battery anodes. *J. Mech. Phys Solids* **2011**, *59*, 1717.